Chapter 5

Result and Discussions

CORROSION AND TRIBOLOGICAL BEHAVIOUR OF SINTERED ALLOY

5.1 Introduction

This chapter of the thesis is exclusively focused on studying the effect of microstructure and mechanical properties on the corrosion and tribological behavior of Ti-5Cu-xNb alloys in simulated body fluid solution at room temperature. The study of the Electrochemical techniques (open circuit potential, electrochemical impedance spectroscopy, and potentiodynamic polarization) was used to investigate the corrosion confrontation behavior of the alloys in the presence of simulated body fluid (pH- 7.4) solution at room temperature. Simultaneously, the tribological behavior of ternary Ti-5Cu-xNb alloy was first studied against zirconia balls at 10 N, 15 N, and 20 N loads in wet conditions. The detailed investigation of wear parameters like the coefficient of friction, worn surface width, maximum lateral depth, wear rate, wear volume, and wear mechanism were successfully discussed in this study. The exposed surface of the alloys following corrosion testing was thoroughly investigated utilizing the SEM and XPS tests. The FESEM image, EDS, analysis, and scanning probe microscopy image of the worn surface area are discussed in detail. This research suggests that alloy design plays a vital role in analyzing the mechanical and wear properties of Ti alloys for biomedical use.

5.2 Corrosion study

5.2.1 Open-circuit potential

The open-circuit potential relates to the ability of the working electrode with respect to the reference electrode when there is no current supplied, and it reflects the thermodynamic

harmony at the metal-solution intersection as a function of time. The response of the open circuit potential concerning the immersion time of Ti-5Cu, Ti-5Cu-5Nb, Ti-5Cu-10Nb, and Ti-5Cu-15Nb in SBF (pH 7.4) is shown in Fig. 5.1. In the SBF solution, all OCP curves of Ti–Cu and Ti–Cu-Nb sintered alloys shifted higher and subsequently became stable, as shown in Fig. 5.1.

The stable E_{corr} of all four sintered alloys after 1 hr was -136 mV, -144 mV, -106 mV, and +128 mV. The initial E_{corr} for the Ti-5Cu-10Nb alloy is nearly -178 mV (Ag/AgCl). Then it progressively increases to honorable potential attainment after 3600 seconds of immersion to a stable value of approximately -106 mV (Ag/AgCl). Ti-5Cu and Ti-5Cu-5Nb also followed the same variation and reached nobler potential. The OCP curve of Ti-5cu-15Nb started from 50mV and ended at 128mV with significant fluctuation. Besides it, the other three samples were shown lower change and in the negative region from start to end, which offers stability in the corrosive media.

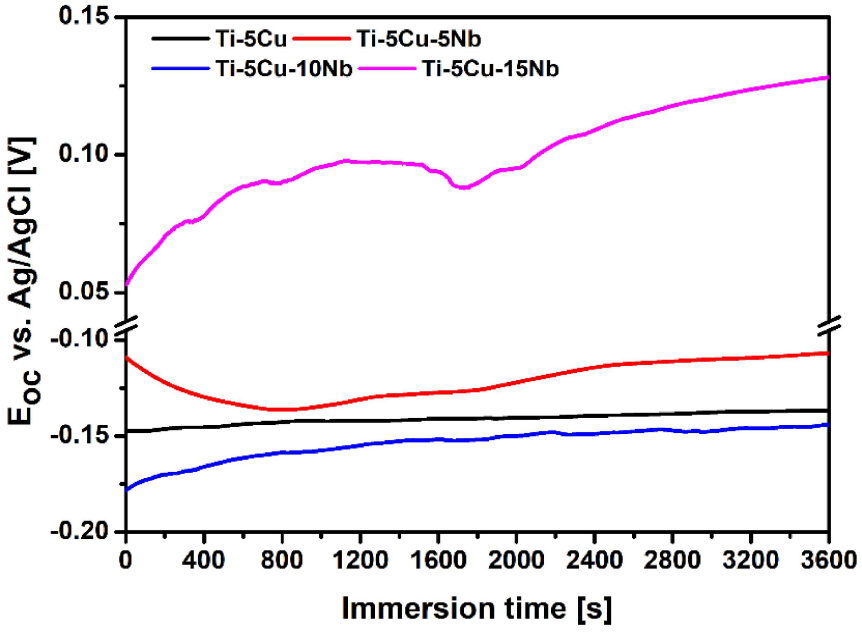

Fig. 5.1- Open-circuit potential test result of the sintered alloys after 3600s

5.2.2 EIS measurements

The result obtained from the EIS test is represented through the Bode-phase plot, and the Nyquist plot is shown in Fig. 5.2 & 5.3, respectively. These diagrams were obtained for the Ti-5Cu and Ti-5Cu-(5-15%) Nb after 3600 seconds of immersion in SBF.

The bode plot shows that the phase angle approaches 70 to 85 degrees in the lower to medium frequency range for three alloys except for Ti-5Cu-15Nb. This indicates a highly capacitive behavior and the formation of a highly stable oxide layer on the surface of the alloy in the solution. This is inconsistent with the low current density obtained in the polarization test. In the higher frequency region (10^3 to 10^5 Hz), the modulus of the impedance of all the alloys becomes constant, associated with a lower phase angle in the bode phase plot indicating a response from solution resistance. Also, from the medium to lower frequency range, the slope of the modulus of Z is nearly -1, which shows that the impedance of the alloy dominates over the resistance of the solution. It could be observed from the bode plot in Fig. 5.2 that profiles of the spectra for Ti-5Cu and Ti-5Cu-5Nb almost touched. This indicates that the corrosion behavior of these two alloys would not change even in lower pH solutions. However, the profile spectra of Ti-5Cu-15Nb are different and come in the lower phase angle. This indicates the less protective passive layer on the surface of the Ti-5Cu-15Nb.

Any specific attribute associated with the electrochemical performance of the Ti-Cu and Ti-Cu-Nb cannot be emphasized using these Bode-phase graphs. Any conclusion based on these EIS graphs should be regarded as speculative. Though, these qualitative experimental data allow us to conclude that all Ti-Cu and Ti-Cu-Nb samples analyzed have similar double-layer deposition and a minimum of two times constant, representing that Ti-5Cu, and all Ti-Cu-Nb alloys experimentally examined have the same corrosion kinetics and titanium oxide layer establishment. Generally, titanium alloy comprises two protective layers: a porous layer and an inner barrier layer (De Assis et al., 2006; Osório et al., 2010; Venugopalan et al., 2000).

Impedance characteristics were estimated using the ZView® tool, utilizing an "equivalent circuit," as shown in Fig. 5.4, to offer quantitative backing for the observed EIS results. The same circuit diagram is also shown by W.R. Osório et al. (Osório et al., 2010) in the EIS test of Ti-Cu in 0.15M NaCl solution and S. L. De Assis (De Assis et al., 2006) in corrosion analysis of Ti-6Al-4V, Ti-6Al-7Nb, and Ti-13Nb-13Zr in Hank's solution.

The oxide layer on Ti-5Cu and Ti-5Cu-(5, 10, 15%) Nb alloys, as per the model, is believed to have a barrier-like inner layer and a porous outer layer, according to the model. In this model, R_s, R_1, and R_2 are the resistance offered by the SBF, outer porous layer, and barrier-like inner layer, respectively. CPE_1 capacitance of the outer porous layer and CPE_2 capacitance of the inner barrier layer. For the sake of simplicity, a constant-phase element representing a change from the ideal capacitor was utilized instead of the capacitance itself.

The impedance of a phase element is represented by the formulae $Z_{CPE} = [C(I\omega)^n]^{-1}$Where C is capacitance, I is current, ω is the frequency, and n lies between -1 to 1. The non-uniform distribution of current caused by roughness and surface imperfections is associated with the value of n (Cremasco et al., 2008; Osório et al., 2007). Table 5.1 shows the solution resistance, capacitance, and n values of the outer-porous and inner-barrier layers, which were calculated by fitting the experimental results using the "equivalent circuit" shown in Fig. 5.4. The value of 'n' near to one shows that the behavior of such a layer was similar to that of a perfect capacitor (Lavos-Valereto et al., 2004). The chi-squared (χ^2) values, which stayed on the order of 10^{-3}, and the error percentages conforming to each component of the proposed circuit (numbers presented in Table 5.1) were used to assess the fitting quality, demonstrating that the data accustomed well to the suggested proposed circuit.

The resistance offered by the outer porous layer of Ti-5Cu-15Nb is 4.04×10^4 Ω cm^2 which is the lowest in comparison to another three alloys. This indicates the Ti-5Cu-15Nb alloy is less stable in the corrosive medium. On the other hand, the resistance offered by the outer porous

layer (R_1) by Ti-5Cu-5Nb is the highest, indicating that the outer porous layer is more resistant to SBF than other alloys. When comparing the capacitances CPE_1 (outer-porous layer) of the Ti-5Cu, Ti-5Cu-5Nb, Ti-5Cu-10Nb, and Ti-5Cu-15Nb using the proposed equivalent circuit, similar tendencies are detected: average values of about 18, 16.1, 27.4, and 36.7 μFcm^{-2} obtained, respectively. However, for all Ti-5Cu, Ti-5Cu-5Nb, Ti-5Cu-10Nb, and Ti-5Cu-15Nb, the CPE_2 (inner-barrier layer) have lesser measured values than the CPE_1. Low capacitances are related to an increase in the thickness of the protective film (Cremasco et al., 2008; De Assis et al., 2006; Osório et al., 2010) and a drop in the dielectric constant of the oxide film (due to changes in the electrolytic solution volume/oxide film ratio)(Cremasco et al., 2008; Gudi et al., 2002; M. Aziz-Kerrzo, K.G. Conroy, A.M. Fenelon, S.T. Farell, 2001). S.L. De Assis et al. (De Assis et al., 2006) showed that the inner-barrier coating delivers corrosion protection, and W.R. Osório et al. (Osório et al., 2010) indicated that both the inner and outer protective layer is responsible for corrosion fortification. In the present study, the lower value of R_2 compared to R_1 for Ti-5Cu, Ti-5Cu-5Nb, and Ti-5Cu-10Nb alloys indicated that the outer porous layer is predominantly responsible for corrosion protection.

Figure 5.3 shows the Nyquist plot of the experimental data obtained by the EIS test of Ti-5Cu, Ti-5Cu-5Nb, Ti-5Cu-10Nb, and Ti-5Cu-15Nb sintered alloys in SBF By comparing the ($Z_{imaginary}$ vs. Z_{real} ratio) of the Ti-5Cu and Ti-5Cu-5Nb sample, the slope of the semi-arc nearly identical as shown in Fig. 5.3. With increasing niobium percentage, the slope also decreases. Based on the discussion and results shown in Table 5.1, the Ti-5Cu, Ti-5Cu-5Nb, and Ti-5Cu-10Nb show better corrosion resistance than Ti-5Cu-15Nb in the simulated body fluid solution. The potentiodynamic anodic polarization performance of the Ti-5Cu, Ti-5Cu-5Nb, Ti-5Cu-10Nb, and Ti-5Cu-15Nb sintered alloys in SBF is evaluated, and the experimental and computed impedance values are approved.

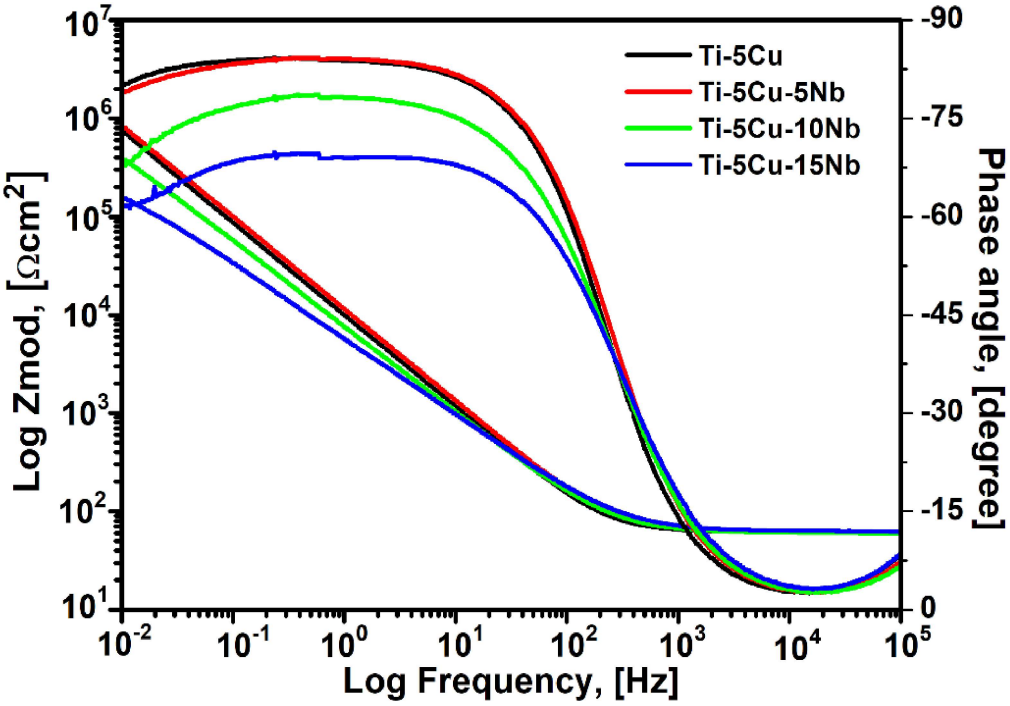

Fig. 5.2- The Bode plot obtained from the EIS test

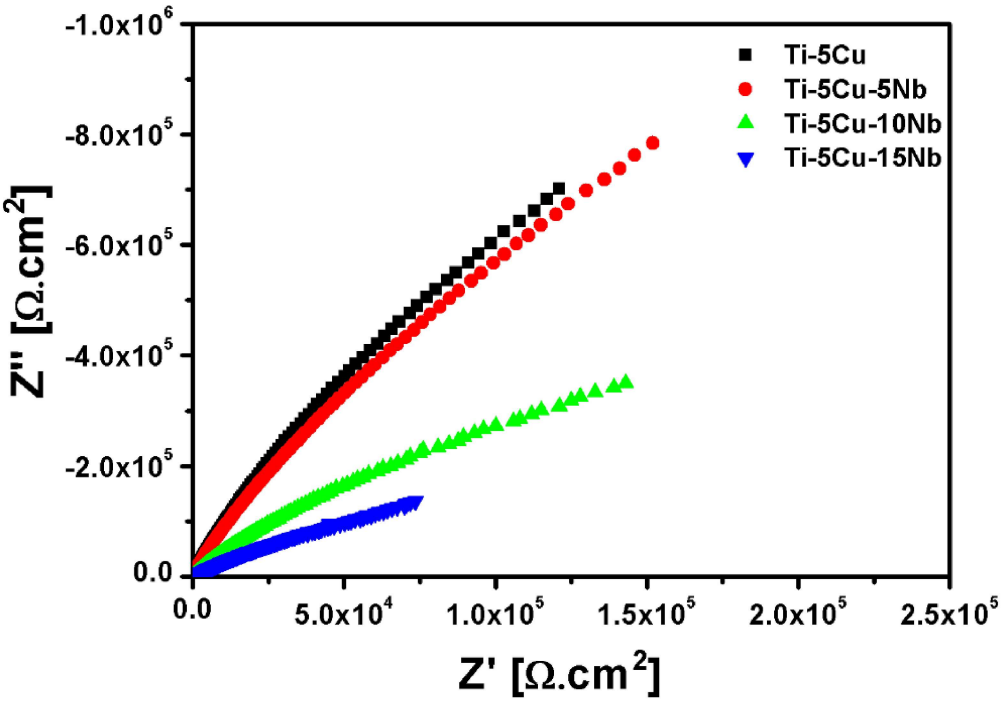

Fig. 5.3- The Nyquist plot obtained from the EIS test

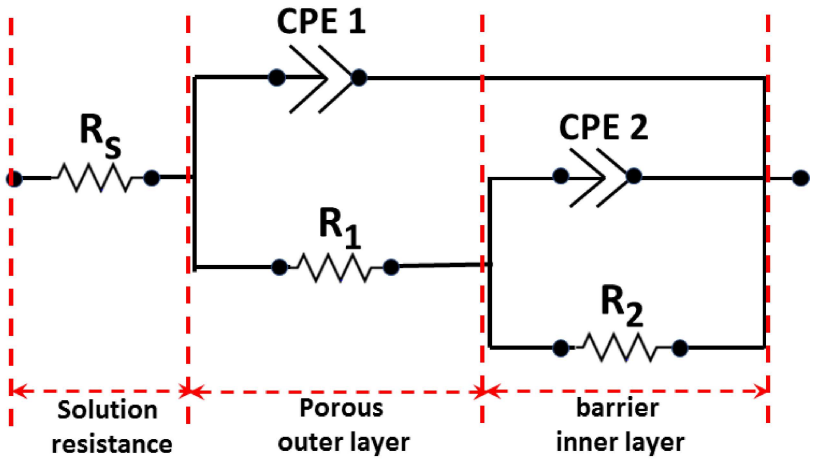

Fig. 5.4- Proposed equivalent circuit diagram of the EIS test after fitting

Table 5.1- Impedance constraints of the proposed equivalent circuit attained by fitting the experimental result of EIS

Sample	R_s (Ωcm^2)	R_1 (Ω cm^2)	CPE_1 ($\mu F cm^{-2}$)	n_1	R_2 (Ω cm^2)	CPE_2 ($\mu F cm^{-2}$)	n_2	χ^2 (10^{-3})
S1	60.95 (0.3)	1.71×10^{12} (6.5)	18.0 (1.5)	0.93	8.97×10^{6} (1.2)	17.6 (2.3)	0.94	5.4
S2	62.27 (0.1)	3.57×10^{12} (10.5)	16.1 (2.3)	0.93	7.45×10^{6} (4.5)	15.4 (3.5)	0.94	6.9
S3	59.83 (0.2)	2.10×10^{12} (14.2)	27.4 (2.8)	0.86	1.78×10^{6} (1.8)	26.1 (1.6)	0.88	7.0
S4	61.76 (0.4)	4.04×10^{5} (4.5)	36.7 (4.5)	0.80	1.01×10^{6} (2.3)	42.7 (8.5)	0.76	8.0

The percent difference derived from fitting for each component of the analogous circuit is given in parentheses.

5.2.3 Potentiodynamic polarization behavior

The potentiodynamic polarization results of Ti-5Cu, Ti-5Cu-5Nb, Ti-5Cu-10Nb, and Ti-5Cu-15Nb alloys in SBF solutions are shown in Fig. 5.5. Polarization parameters, including corrosion potential (E_{corr}), corrosion current density (i_{corr}), breakdown potential, passive current density (i_{pp}), and re-passivation current density, were attained using standard procedures from the potentiodynamic polarization graphs, as listed in Table 5.2. The anodic and cathodic slopes of the Tafel plot were considered for calculating corrosion potential and current density. The intersection point of the slope of the anodic and cathodic curves decides the E_{corr} and i_{corr} values.

From the OCP value of the Tafel plot, +50 mV was added to the anodic side, and a -50 mV value was added to the cathodic side. Then the slopes from these points were taken into consideration. The primary polarization current (i_{pp}), breakdown potential, and re-passivation current were obtained directly from the anodic branch of the Tafel plot.

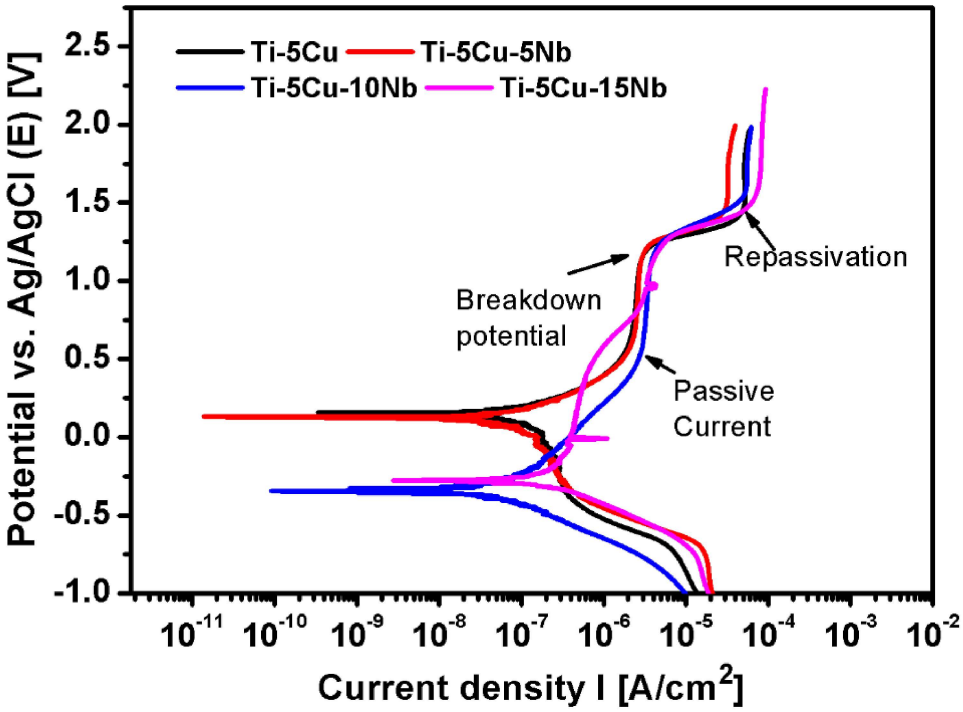

Fig. 5.5- Potentiodynamic polarization curve of sintered alloys.

Table 5.2- Corrosion current density, corrosion potential, breakdown potential, passive current, and repassivation current of the sintered alloys

Parameters	Ti-5Cu	Ti-5Cu-5Nb	Ti-5Cu-10Nb	Ti-5Cu-15Nb
Corrosion Current density i_{corr} [nA cm^{-2}]	40.12(±3.12)	31.07(±4.17)	21.44 (±2.15)	106.37(±11.32)
Corrosion Potential E_{corr} [mV]	143(±10)	11.7(±2)	-339(±14)	-277(±17)
Breakdown Potential [mV]	1155(±20)	1155(±20)	1146 (±25)	1274 (±30)
Passive Current density [µA cm^{-2}]	2.07(±0.58)	2.25(±.89)	2.83(1.01)	3.02(±1.14)
Repassivation Current [µA cm^{-2}]	51.7(±8.1)	30.4(±4.15)	51.5(±14.2)	71.5(±21.65)

The corrosion potential (E_{corr}) obtained from the polarization is slightly different from open

circuit potential measurements. This is expected, as the polarization measurements started at a cathodic potential (-1.6 V to OCP) so that the E_{corr} (polarization) increases for Ti-5Cu and Ti-5Cu-5Nb and decreases for Ti-5Cu-10Nb and Ti-5Cu-15Nb. This deviation in the potential reduces the passive film at the surface due to highly reducing initial potentials. It can be observed from the Tafel plot that the i_{corr} value reduces with increasing niobium weight percent up to 10% and sudden increases for 15% weight fraction, shown in Table 5.2. The slope of the anodic branch for Ti-5Cu and Ti-5Cu-5Nb is approximately the same, but Ti-5Cu-10Nb and Ti-5Cu-15Nb are not the same as the other two. The faster growth of the potential from E_{corr} for the Ti-5Cu-10Nb indicates that the passive layer is slightly replaced by the less protective film, which becomes stable at 2.83×10^{-6} (A/cm^2) current density. This point is called passive current density(i_{pp}). The passive current density for all the sintered alloys is in the range of nearly (2 to 3 $\mu A\text{-}cm^{-2}$), the lowest for Ti-5Cu and the maximum for Ti-5Cu-15Nb. The highest value of the i_{pp} of the Ti-5Cu-15Nb indicates a defect in the oxide film and the formation of the more irregular porous protective layer. At around 1.17×10^{-7} (A/cm^2), the potential for Ti-5Cu-15Nb starts to increase faster and then becomes stable at -3.7 mV. The current density oscillation shows that the passive film is breaking down at this moment, similar to the situation during pitting formation and re-passivation. However, the breakdown potential of the all-sintered alloy is nearly the same. All the sintered alloys show the re-passivation at around (1500 to 1550 mV to Ag/AgCl). After the first breakdown of the first protective layer, the new layer formed suddenly, and it became stable till the remaining applied potential. The corrosion rate directly relates to the corrosion current density; as shown in Table 5.2, the current density of the Ti-5Cu decreases with increasing niobium percentage up to 10 %. The Ti-5Cu-15Nb has a higher percentage of niobium; thus, β-Ti stabilizes more than $\alpha+Ti_2Cu$; thus, the corrosion potential decreases rapidly compared to the other three alloys. In earlier research, J. Wang et al. (J. Wang et al., 2019) also reported that transformed β-Ti causes a negative influence on the

corrosion susceptibility of Ti-5Cu alloys. In the present study, the i_{corr} value of Ti-5Cu-10Nb (21.44 nA cm^{-2}) lies between the i_{corr} value of Ti-13Nb-13Zr, and Ti-6Al-4V (De Assis et al., 2006) when tested in naturally aerated Hank's solution. Based on the above results, the present study concluded that the addition of niobium enhances the corrosion potential of Ti-5Cu alloys in SBF compared to i_{corr} value recent research of Ti-Cu alloys (Pina et al., 2016; Tao et al., 2020; E. Zhang et al., 2013, 2016b).

5.2.4 Surface Analysis

Figure 5.6 (a-d) shows the typical SEM microstructure of the Ti-5Cu, Ti-5Cu-5Nb, Ti-5Cu-10Nb, and Ti-5Cu-15Nb sintered alloys after the potentiodynamic polarization test in SBF. The surface morphology of Ti-5Cu in Fig. 5.6 (a) indicates that some localized corrosion takes place along with many corrosion micro-pits are also observed. In Fig. 5.6 (b), the corroded surface of Ti-5Cu-5Nb revealed the formation of the oxides layer, which protected the alloys during anodic corrosion. This layer reduces the localized corrosion and micro-pits compared to Fig. 5.6 (a). The SEM image of Ti-5Cu-10Nb in Fig. 5.6 (c) has less oxide formation than Ti-5Cu and Ti-5Cu-5Nb. The corrosion current density (i_{corr}) of Ti-5Cu-15Nb is maximum, as shown in Table 5.2, and the SEM image, as shown in Fig 5.6 (d), proved the same. The entire surface affected by the corrosion and very rough surface, along with macro-pits, is shown in the image. Ti-5Cu-15Nb corroded more badly compared with the other three alloys in SBF. The α+Ti_2Cu and α+transformed β-Ti phases are mainly responsible for protecting against chemical attacks(J. Wang et al., 2019). The XRD and SEM results show that the volume fraction of β-Ti is highest in Ti-5Cu-15Nb, and this might be the possible reason for the poor anti-corrosion property of this alloy.

In the previous study, the corroded SEM image of Ti-Ag in artificial saliva reported by B. B. Zhang et al. (B. B. Zhang et al. 2009) showed nearly the same as in the present study. The surface of the corroded Ti-Nb alloy is mainly composed of TiO_2 and Nb_2O_5, as shown by Y. J.

Bai et al. (Bai et al., 2011) when tested in various electrolytes composed of artificial saliva and modified artificial saliva solution. In the present study, the same compound formed on the alloys' surface, which was further proved by the XPS study.

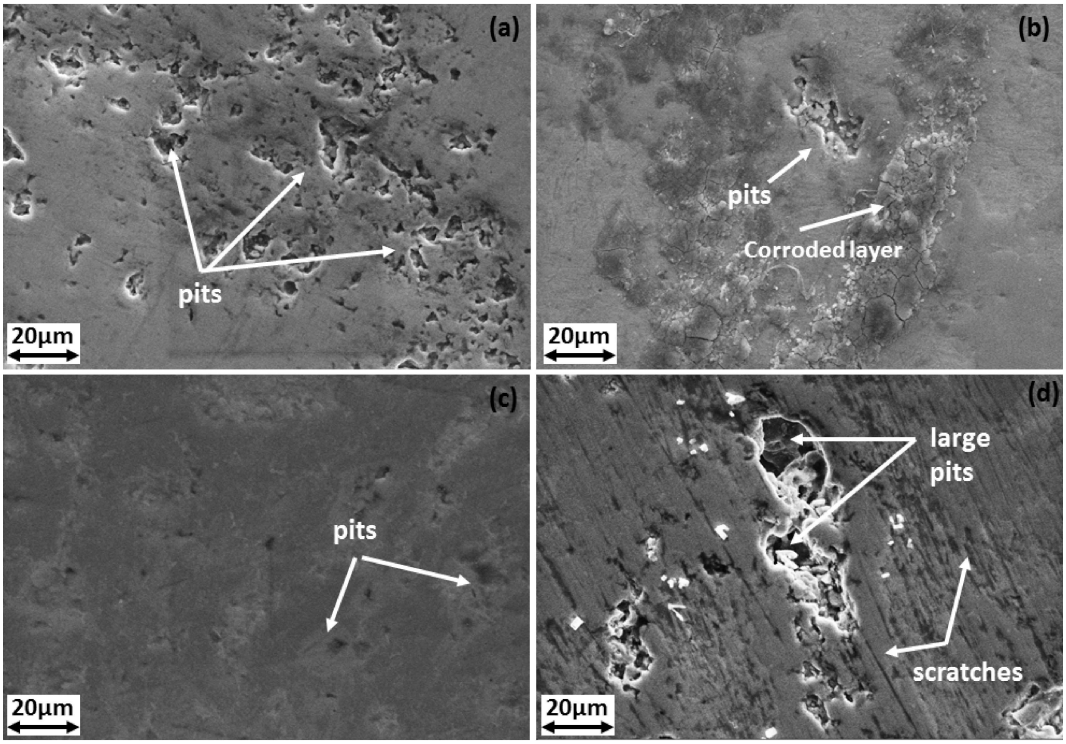

Fig. 5.6- SEM image of the corroded sample (a) Ti-5Cu, (b) Ti-5Cu-5Nb, (c) Ti-5Cu-10Nb, and (d) Ti-5Cu-15Nb sintered alloys

Figures 5.7 and 5.8 show the XPS spectra of corroded surfaces of all the alloys after the potentiodynamic corrosion test to know the phases and oxide compounds formed after corrosion. The XPS spectra revealed that the main composition of the surface layer of Ti-5Cu, Ti-5Cu-5Nb, Ti-5Cu-10Nb, and Ti-5Cu-15Nb alloys after tests in SBF were TiO_2, CuO, and Nb_2O_5. The chemical bonds of O1s for Ti-5Cu, Ti-5Cu-5Nb, Ti-5Cu-10Nb, and Ti-5Cu-15Nb were determined as shown in Fig. 5.8 (a): oxygen was present at the surface of Ti-5Cu, Ti-5Cu-5Nb, Ti-5Cu-10Nb, and Ti-5Cu-15Nb with binding energies of E_b = 530.47 eV, 530.47 eV 530.27 eV, and 530.87 eV, respectively. The binding energy of TiO_2 was also shown in

Fig. 5.8 (b) as 458.87 eV, 458.87 eV, 459.07, and 458.87, respectively. The binding energy of Nb_2O_5 for Ti-5Cu-5Nb, Ti-5Cu-10Nb, and Ti-5Cu-15Nb are 207.38 eV, 207.87 eV, and 207.38 eV, respectively. Both copper and niobium are known for the enhancement of corrosion resistance.

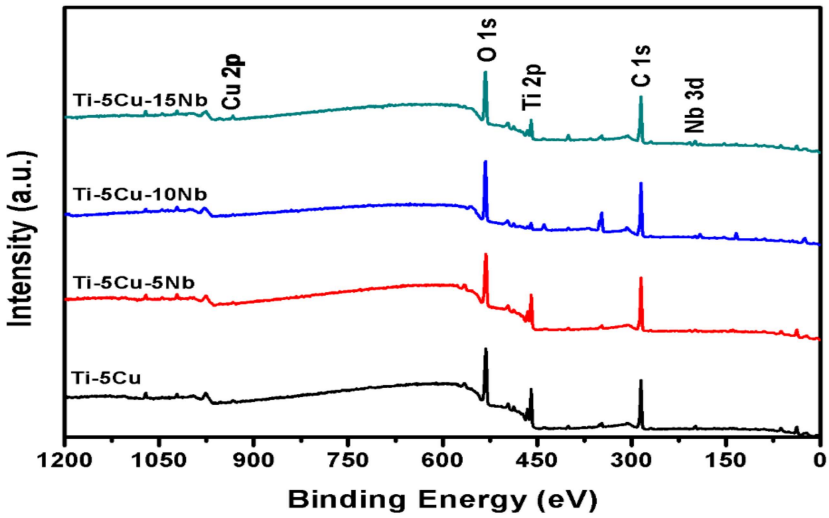

Fig. 5.7- XPS spectra of the sintered alloy after the potentiodynamic polarization test

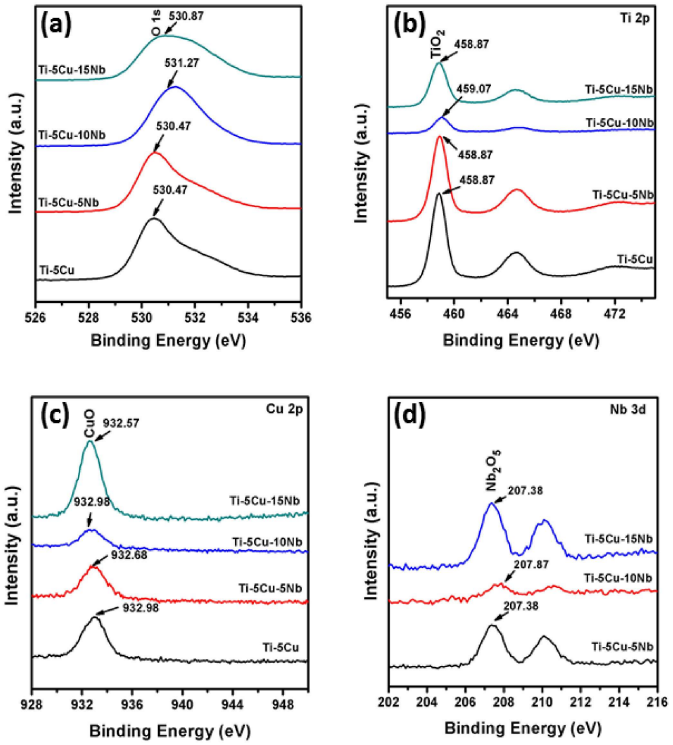

Fig. 5.8- XPS spectra of the element (a) Oxygen, (b) Titanium, (c) Copper, and (d) niobium. Copper formed CuO compound with oxygen with higher bind energy of 932.98 eV, 932.68 eV, 932.98 eV, and 932.57 eV, respectively.

The open-circuit potential measurements, electrochemical impedance spectroscopy studies, and polarization tests were all in agreement with the SEM and XPS studies.

5.3 Wear and frictional behavior of alloys

5.3.1 Coefficient of friction

Figure 3.9 depicts the schematic diagram of the wear study and the worn profile of samples in wet conditions against zirconia ball.

Figure 5.9 shows the coefficient of friction vs. running cycle of Ti-5Cu-(0, 5, 10, and 15% Nb) at 10 N, 15 N, and 20 N load, respectively. In Fig. 5.9 (a), the cof value of Ti-5Cu at 10 N load attained a maximum value of 0.71 shortly after the experiment started and became steady after 1000 cycles. A similar variation in cof value was obtained at 15N load; also, the maximum cof reached slightly lower than the 10 N load. However, at 20 N load, the maximum cof attained a value of 0.48 at the initial stage, and it remained steady after completing 150 cycles. Accordingly, the maximum and minimum cof values were attained at 10 N and 20 N loading, respectively. The average cof values at 10 N, 15 N, and 20 N loads were 0.506±0.061, 0.515±0.034, and 0.402±0.028, respectively, for the 3600 cycles. Ti-5Cu-5Nb followed the same tendency of maximum and minimum cof values for 10 N and 20 N loading, as shown in Fig. 5.9 (b). The average cof value 0.302±.0041, 0.252±0.044, and 0.227±0.046 were obtained at 10 N, 15 N, and 20 N loads. The cof vs. running cycle plot of Ti-5Cu-10Nb, as shown in Fig. 5.9 (c), reveals that the alloy obtained a maximum cof value at a 15 N load with an average cof value of 0.665±0.067, while the minimum cof value at 10 N load with an average of 0.505±0.068. The average cof value increases by 31.68 % at 15 N load compared to 10 N load. The cof value of Ti-5Cu-15Nb with respect to the running cycle shows a relatively constant value throughout the whole running period, as shown in Fig. 5.9 (d). The average cof 0.367±0.022, 0.311±0.012, and 0.506±0.023 were gained at 10 N, 15 N, and 20 N load,

respectively, as depicted in Fig. 5.10. The cof value against sliding distance for Ti-5Cu-10Nb, and Ti-5Cu-15Nb shows an unstable or fluctuating profile at all three loading conditions. Based on the average cof value, Ti-5Cu-5Nb is less prone to wear than the other three samples, while Ti-5Cu-15Nb is more favorable to wear against its zirconia counterpart in SBF.

The friction coefficient depends on the magnitude of the load, surface condition, and the relative hardness of mating parts (Uthayakumar et al., 2013). In Fig. 5.9 (a) and (b), increasing the load reduces the average coefficient of friction; at the early stage, the alloy structure is slightly pressed. During the second stage, some particles slowly disengage at the two points of interaction, and more and more particles detach with increasing load (Xu et al., 2013). The loose particles or wear debris acts as a lubricant between mating zirconia ball and samples. However, this trend is not the same for the average cof value of Ti-5Cu-10Nb, and Ti-5Cu-15Nb, as shown in Fig. 5.9 (c) & (d). The worn surface SEM image of Ti-5Cu-10Nb at 15 and 20 N load shows the presence of grooves, delamination, and adhesion through the exposed area. The presence of these irregularities might be the possible reason for the maximum average cof value at a higher load (Doni et al., 2013). Xu LJ et al.(Xu et al. 2013) also reported that 5% Nb showed a lower coefficient of friction than 10 %, 15 %, and 20% Nb in Ti-15Mo alloy; the same average cof value was also observed in this investigation.

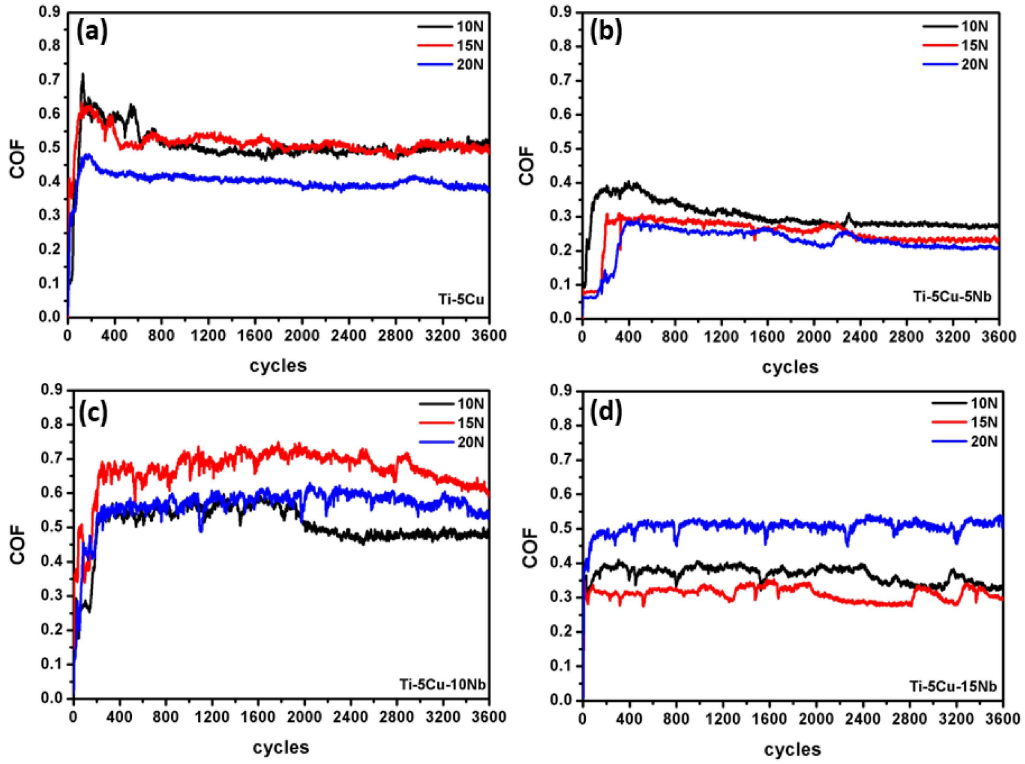

Fig. 5.9- Coefficient of friction vs. running cycles of samples (a) Ti-5Cu, (b) Ti-5Cu-5Nb, (c) Ti-5Cu-10Nb, and (d) Ti-5Cu-15Nb at 10 N, 15 N, and 20 N loads, respectively.

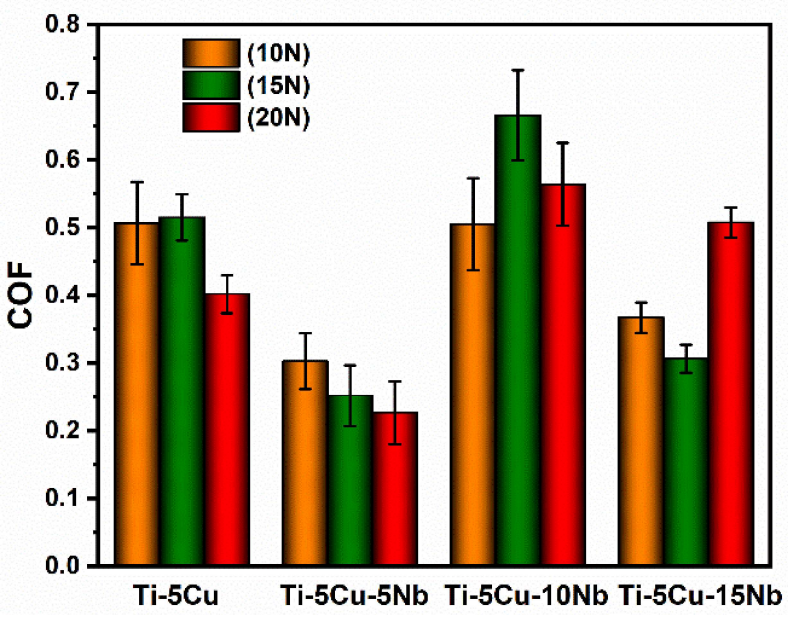

Fig. 5.10 - Average friction coefficient of sintered alloys running after 3600 cycles at 10 N, 15 N, and 20 N load, respectively.

5.3.2 Worn surface width and lateral depth

The wear scar profile measured by profilometer of samples Ti-5Cu, Ti-5Cu-5Nb, Ti-5Cu-10Nb, and Ti-5Cu-20Nb is demonstrated in Fig. 5.11 and 5.12, in which the wear area of the 2D profile and maximum lateral depth are quantified and calculated. Compared to the wear track profiles at 15 N and 20 N loading conditions, the wear track profile of Ti-5Cu at 10 N load is not considerably smooth. Furthermore, the worn surface profile of Ti-5Cu-5Nb at 10 N and 15 N loads is not as uniform as at 20 N loads. It is due to the accumulation of wear particles on the worn surface. The maximum depth and lateral width of the wear scar are reported in Table 5.3.

On the other hand, the smooth surface has the lowest coefficient of friction, but the wear volume loss is more significant than the non-smooth surface. The same result of volumetric wear loss of smooth surface can be seen in Table 5.3. At 20 N load, the worn surface profile became wider and deep for Ti-5Cu-5Nb, resulting in the highest wear loss and worst wear resistance (Fig. 5.11 f). As shown in Fig. 5.12, the worn surface profile of Ti-5Cu-10Nb and Ti-5Cu-15Nb against the zirconia ball differs from Fig. 5.11. Although the width of the worn surface increases with increasing load for Ti-5Cu-10Nb compared to Ti-5Cu and Ti-5Cu-5Nb, this trend does not apply with Ti-5Cu-15Nb. As illustrated in Fig. 5.13 (a), the wear track width of Ti-5Cu-15Nb is less than Ti-5Cu-10Nb for 10 N, 15 N, and 20 N loads. The wear track width of sample Ti-5Cu-10Nb was recorded 1181 μm and 1227 μm for 15 N and 20 N loads, respectively, which was the widest of all the samples. The maximum lateral depth of the worn profile was obtained for Ti-5Cu-15Nb at 20 N load.

Figure 5.13 (b) depicts the maximum lateral depth of worn surfaces measured by the profilometer for all four samples under three loading conditions. Ti-5Cu-10Nb recorded maximum depths of 17.3 μm and 21.2 μm under 10 N and 15 N loads, respectively. Also, at 20 N loads, the wear depth increases as the niobium percentage to Ti-5Cu increases, reaching

a maximum of 26.6 μm for Ti-5Cu-15Nb. As illustrated in Fig. 5.9, the average cof value of Ti-5Cu-10Nb at 10 N, 15 N, and 20 N loads are maximum compared to the other three samples. The same trend we can observe in Fig. 5.13 (a) and (b). Higher cof values for Ti-5Cu-10Nb at 10 N and 15 N loads exacerbated the lateral maximum depth and width simultaneously to wear track, but at 20 N load, the counter material mainly increases width, not depth. Based on this finding, it can be concluded that increasing the load or stress applied to the Ti-5Cu-15Nb will reduce the lateral penetration and widen the wear track. At three loading conditions, Ti-5Cu had the smallest breadth and lateral depth of wear track of all the samples, indicating that it is more wear-resistant.

The depth and width of the wear track largely depend upon the material hardness, density, microstructure, and elastic modulus (Fellah et al., 2013). The wear depth of the material depends upon the hardness of the counter material (Iijima et al., 2003). As it is observed in the previous study (Pandey et al., 2022), the Vicker micro-hardness value of Ti-5Cu is the highest compared to the other three samples. Also, the maximum depth of the worn surface increases with increasing loads and niobium percentage in Ti-5Cu. Compared to Ti-5Cu, the maximum depth and waviness are highest for Ti-5Cu-5Nb. However, the cof value is the lowest for Ti-5Cu-5Nb. The wear debris between the mating part acts as a lubricant and lowers the cof compared to Ti-5Cu.

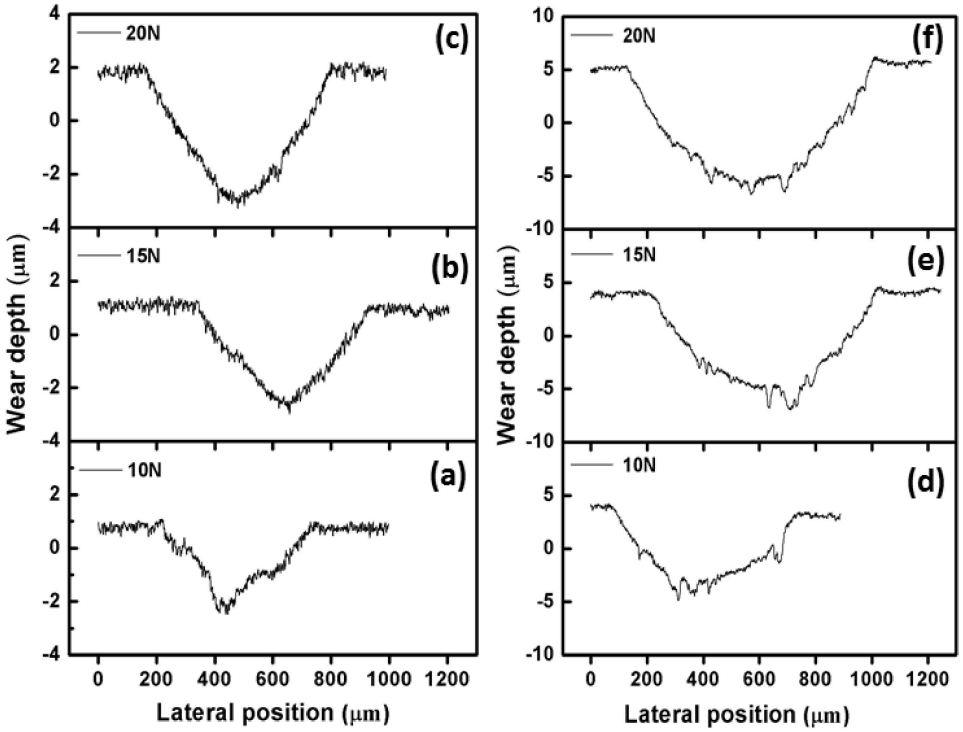

Fig. 5.11 - Measurement of the worn surface by profilometer (a, b, and c) of Ti-5Cu, and (d, e, and f) of Ti-5Cu-5Nb at 10N, 15N, and 20N load, respectively

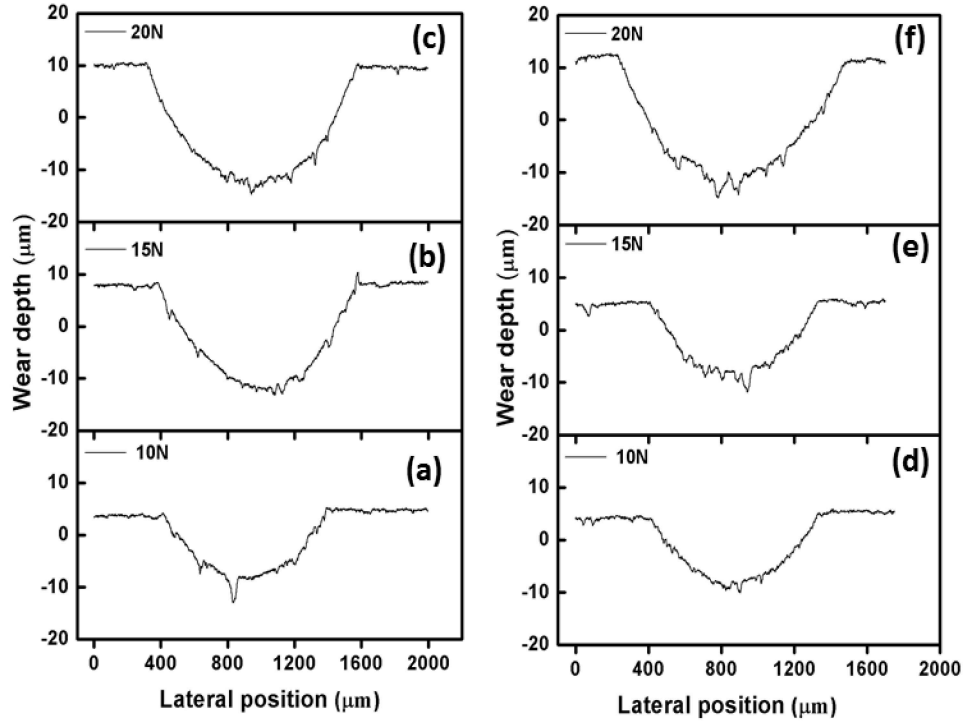

Fig. 5.12- Measurement of worn surface by profilometer (a, b, and c) of Ti-5Cu-10Nb, and (d, e, and f) of Ti-5Cu-15Nb at 10 N, 15 N, and 20 N load.

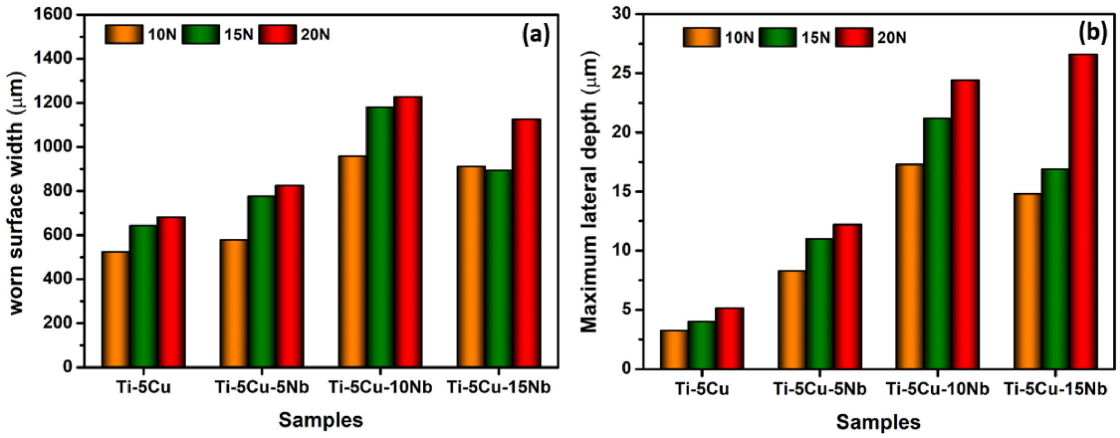

Fig. 5.13- Width and lateral depth of worn surfaces at all three loadings against zirconia ball.

5.3.3 Wear volume and wear rate

Wear volume and wear rate are evaluated using equations 2 and 3 (chapter 3) based on the result finding of wear track width and average lateral depth. The wear rate varies with load and sample compositions, as shown in Fig. 14. Table 5.3 shows that at 10N load, Ti-5Cu-10Nb has a maximum wear rate of $6.19239\times10^{-7}(mm^3/mm)$, while Ti-5Cu has a minimum wear rate of $5.35916\times10^{-8}\,(mm^3/mm)$. The wear rate increased by approximately 10.5 times with adding 10 wt. % niobium to Ti-5Cu at 10N load against zirconia counter material. Furthermore, Ti-5Cu-15Nb has shown 3.5% lower wear rate than Ti-5Cu-10Nb under the same loading conditions. The wear rate at the 15 N loading condition follows the same pattern for all samples. Moreover, at 20 N load, the wear rate continuously increased with increasing niobium to Ti-5Cu and reached the maximum value of $1.44976\times10^{-6}(mm^3/mm)$ in SBF against the zirconia ball. Based on these wear rate data, Ti-5Cu has outstanding anti-wear properties against zirconia balls, whereas niobium inclusion in Ti-5Cu has a negative impact on strength in reciprocating motion.

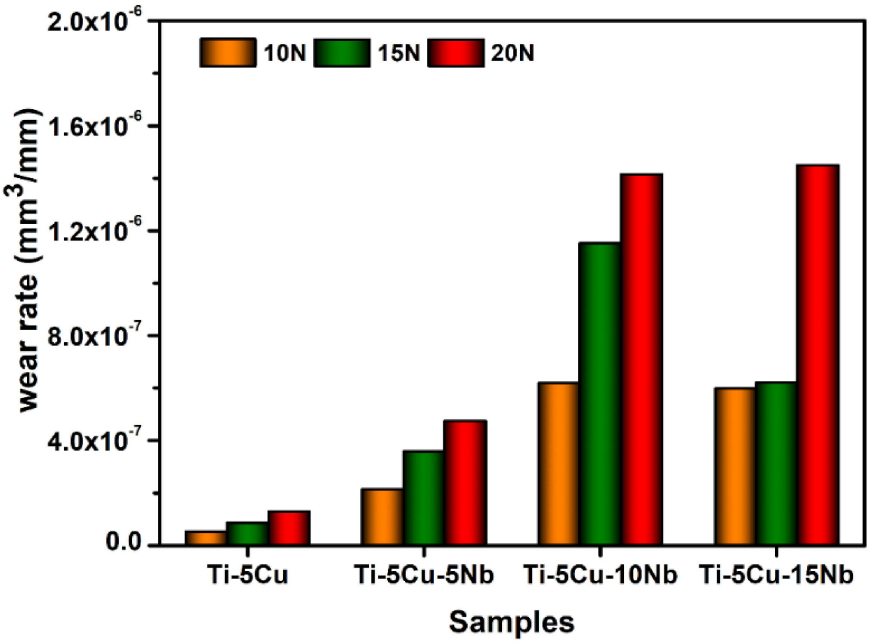

Fig. 5.14- Wear rate of all four samples running after 3600 cycles against zirconia ball in SBF.

Table 5.3- Parameter and results obtained after wear test of the samples in SBF.

Sample	Load (N)	Wear scar width (µm)	Max. lateral depth (µm)	Volumetric wear × 10^{-3}(mm^3)	Wear rate × 10^{-8}(mm^3/mm)
Ti-5Cu	10	523	3.24	3.85	5.36
	15	642	4.01	6.20	8.61
	20	681	5.14	9.28	12.88
Ti-5Cu-5Nb	10	579	8.27	15.49	21.51
	15	777	11.01	25.83	35.87
	20	825	12.20	34.11	47.38
Ti-5Cu-10Nb	10	959	17.30	44.58	61.92
	15	1181	21.20	82.98	115.25
	20	1227	24.40	101.81	141.41
Ti-5Cu-15Nb	10	911	14.80	42.98	59.70
	15	894	16.90	44.64	62.00
	20	1126	26.60	104.38	144.97

The wear rate mainly depends on the mechanical properties (hardness, density, elastic modulus, load applied, and Hertzian contact pressure) of substrate material and the hardness of counterpart material. The wear rate mainly depends on the H/E (hardness/elastic modulus) ratio

(Ehtemam-Haghighi et al., 2016a). The hardness and elastic modulus of the alloys were calculated and given in our previous study; the H/E ratio of the alloy decreases with increasing niobium percentage. This might be the main reason behind the increasing wear rate of the alloy against the zirconia ball. The SEM image of the microstructure of the alloys and volume fraction of phases indicates the formation of the beta phase with increasing niobium percentage. The higher beta phase is less stable in mechanical abrasion, and the breakdown of passive layers continuously occurs. Ehtemam-Haghighi S (Ehtemam-Haghighi et al., 2016a) showed in their research that the maximum beta phase is responsible for the increased wear rate of the alloys. Although the wear rate of the samples used in this study is increasing with niobium addition, this is relatively less than in other earlier studies. The maximum loading condition and lesser density of the samples with niobium addition might be the main reason behind the higher wear rate.

5.3.4 Worn surface characterization

Figure 5.15 shows the scanning electron microscopy (SEM) image and energy dispersive X-ray spectroscopy (EDS) analysis of the worn surfaces of Ti-5Cu at three loading conditions. The average cof value of Ti-5Cu alloy at 15 N load is maximum compared to 10 N and 20 N load (Fig. 5.10), and the scratches in SEM images of the worn surfaces reveal the same. The possible reason for maximum scratches is the early breakdown of the passive oxide layer, which resulted in direct contact between the zirconia ball and the alloy surface. The worn surface image of Ti-5Cu at 20 N load has minimum oxide and the adhesive layer, resulting in the minimum average cof value during the whole cycle compared to other loading conditions. The width of the worn surface follows the loading condition and increases with increasing load, as shown in Fig. 5.15. The maximum width of the wear track was observed at 20 N load, which is 30 % more than the width at 10 N load. Moreover, surface delamination was also observed at the 15 N loading of Ti-5Cu. The EDS analysis of the selected area shows the presence of O,

Ti, and Cu.

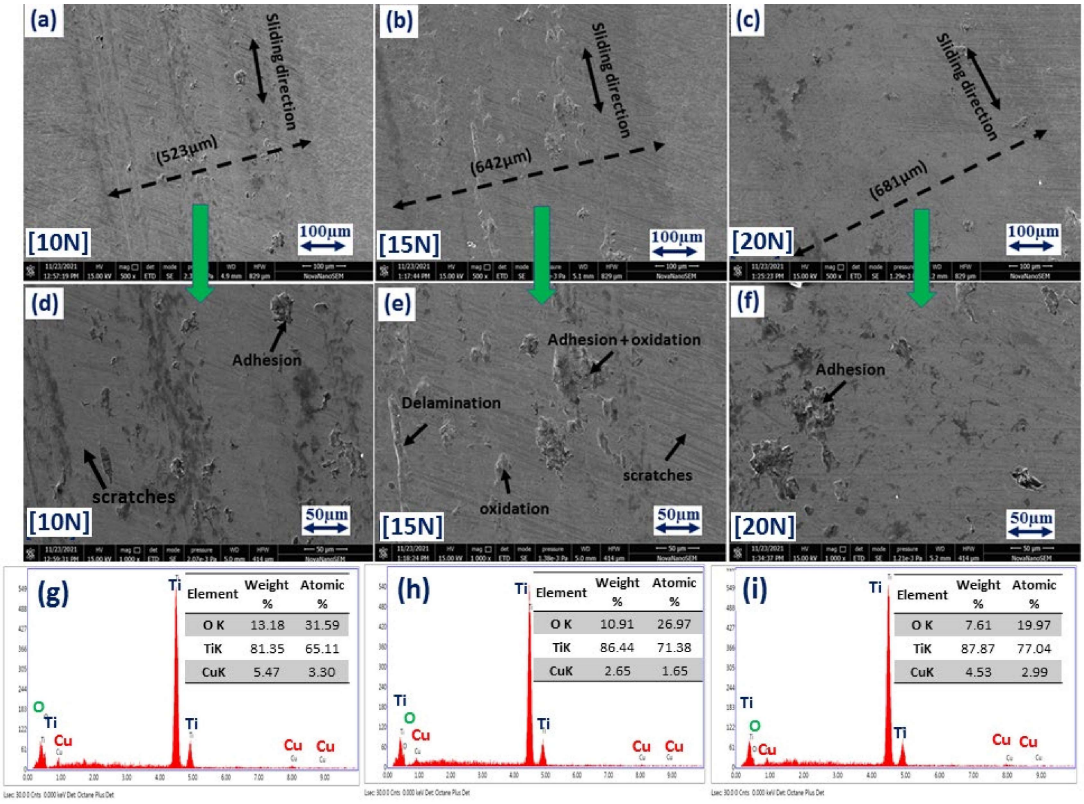

Fig. 5.15- The SEM image and EDS analysis of the worn surface of Ti-5Cu at 10 N (a,d,g), 15 N (b,e,h), and 20 N (c,f, i) load after 3600 cycles.

Figure 5.16 shows the SEM image of the worn surface of Ti-5Cu-5Nb at different loading conditions, and the EDS report of the selected area is shown in Fig. 5.16 (d, e, and f). As shown in Fig. 5.9 (b), the cof value decreases with increasing load; the same pattern can also observe in the SEM image of worn surfaces (Fig. 5.16). Figure 5.16 (a) has maximum whitish and black debris of oxides as compared to Fig. 5.16 (b) and (c), which causes the maximum cof value. With increasing load, the cof value decreases accordingly while the wear track width increases. The EDS report of the selected region of Fig. 5.16 (d, e, and f) shows the presence of O, Ti, Cu, and Nb.

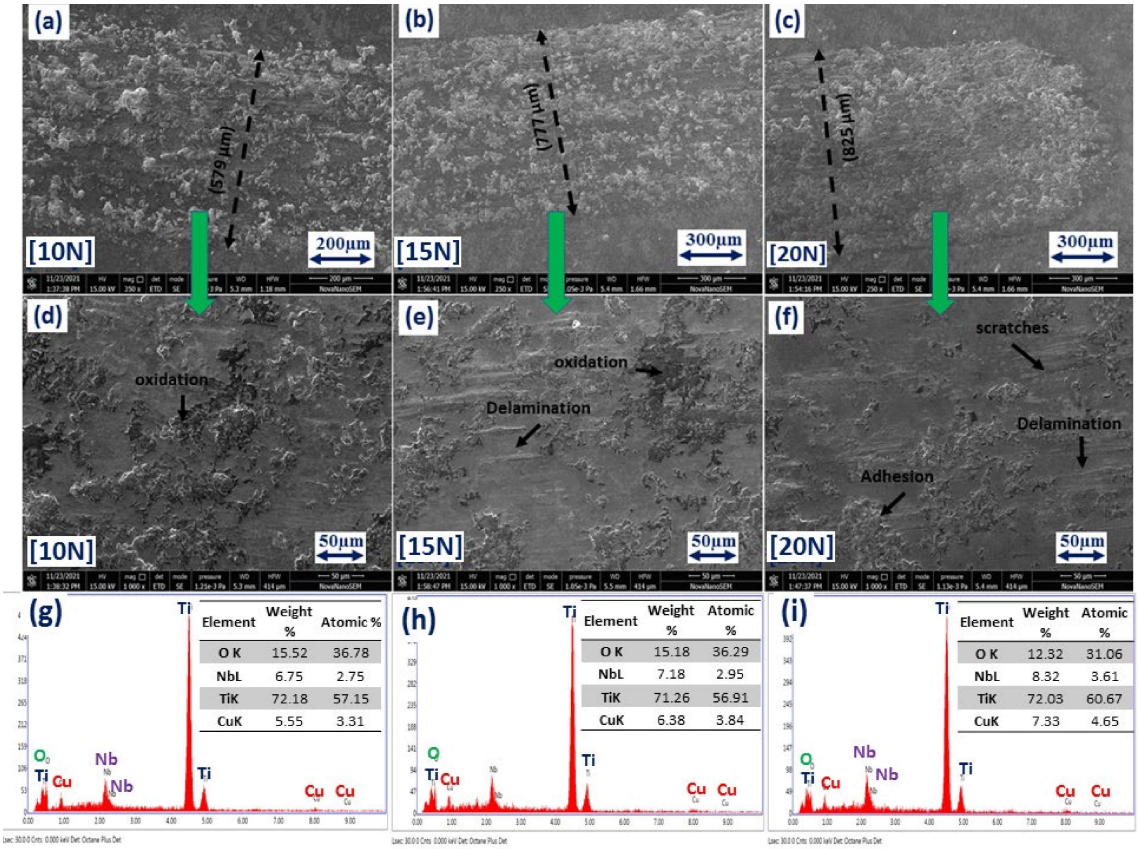

Fig. 5.16- The SEM micrograph and EDS analysis of the worn surface of Ti-5Cu-5Nb at 10 N (a,d,g), 15 N (b,e,h), and 20 N (c,f, i) load after 3600 cycles.

Figure 5.17 shows the SEM image and EDS analysis of worn surfaces of Ti-5Cu-10Nb against the zirconia ball in SBF. All the samples exhibit typical indications of adhesion with a few disparities. The correlation between the presence of niobium in EDS, the SEM image, and the cof value can be observed in Fig. 5.17. The maximum cof value was obtained for Ti-5Cu-10Nb at 15 N load, and the corresponding SEM image in Fig. 5.17 (e) shows that oxide layer depletion and surface-to-surface contact of zirconia ball and sample. The lowest niobium presence in the EDS might be the reason for the maximum cof value. Both copper and niobium percent in EDS reports are significantly low, indicating the formation of copper oxide, niobium oxide, and titanium oxide caused by abrasion, adhesion, and excessive temperature between the contact surfaces.

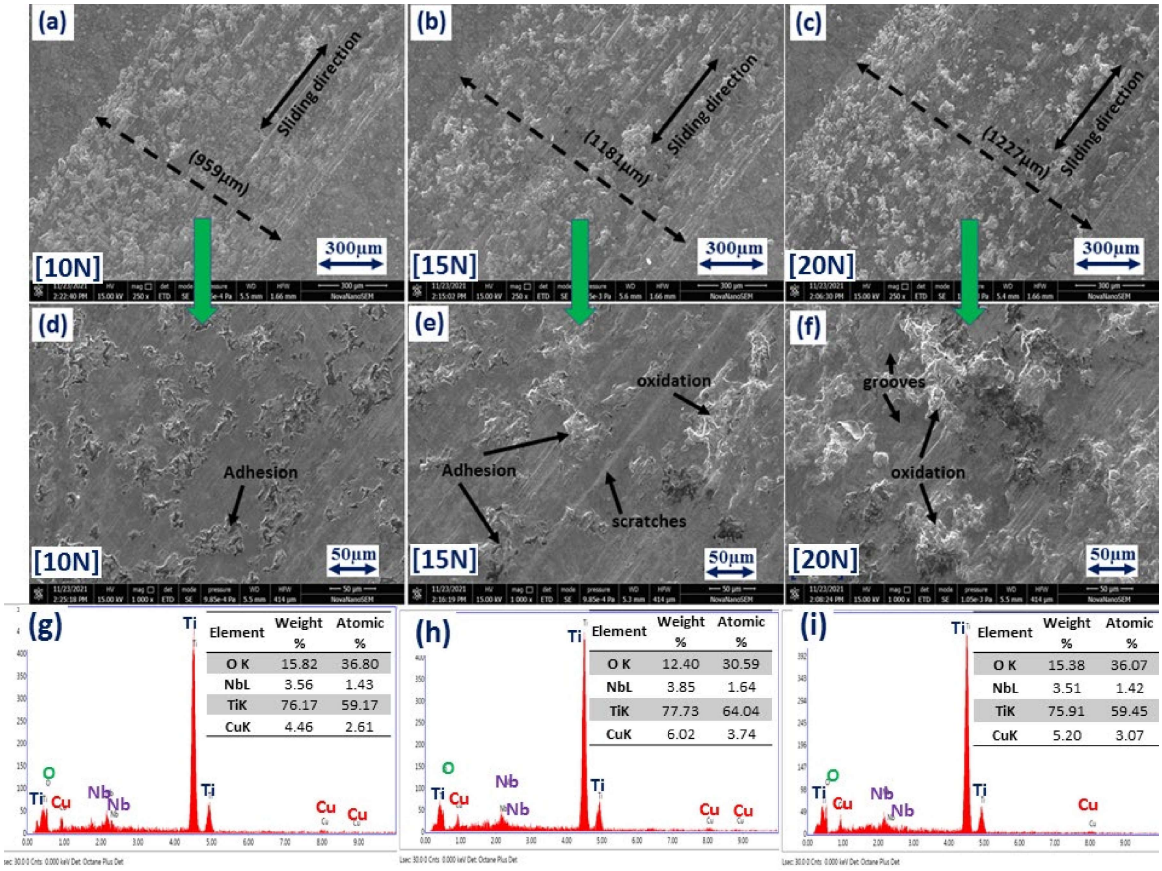

Fig. 5.17 - The SEM micrograph and EDS analysis of the worn surface of Ti-5Cu-10Nb at 10 N (a,d,g), 15 N (b,e,h), and 20 N (c,f, i) load after 3600 cycles.

Figure 5.18 shows the three wear tracks of Ti-5Cu-15Nb at 10 N, 15 N, and 20 N loads. The lowest friction coefficient was obtained for 15 N load and the highest for 20 N load. The worn surface SEM image comprises adhesion, scratches, oxidative layer, and grooves. The width of the wear track was observed to be lower than Ti-5Cu-10Nb, while depth increases comparatively. Also, the existence of grooves in Fig. 5.18 (f) at 20 N loads confirms the higher cof value and maximum lateral depth compared to the cof value and lateral depth at 10 N and 15 N loading conditions. The EDS reports of elements for the 15 N load of Fig. 5.18 (e) are shown in Fig. 5.18 (h). The niobium weight percent compare to other loading is the highest and might be the reason for the lowest friction coefficient.

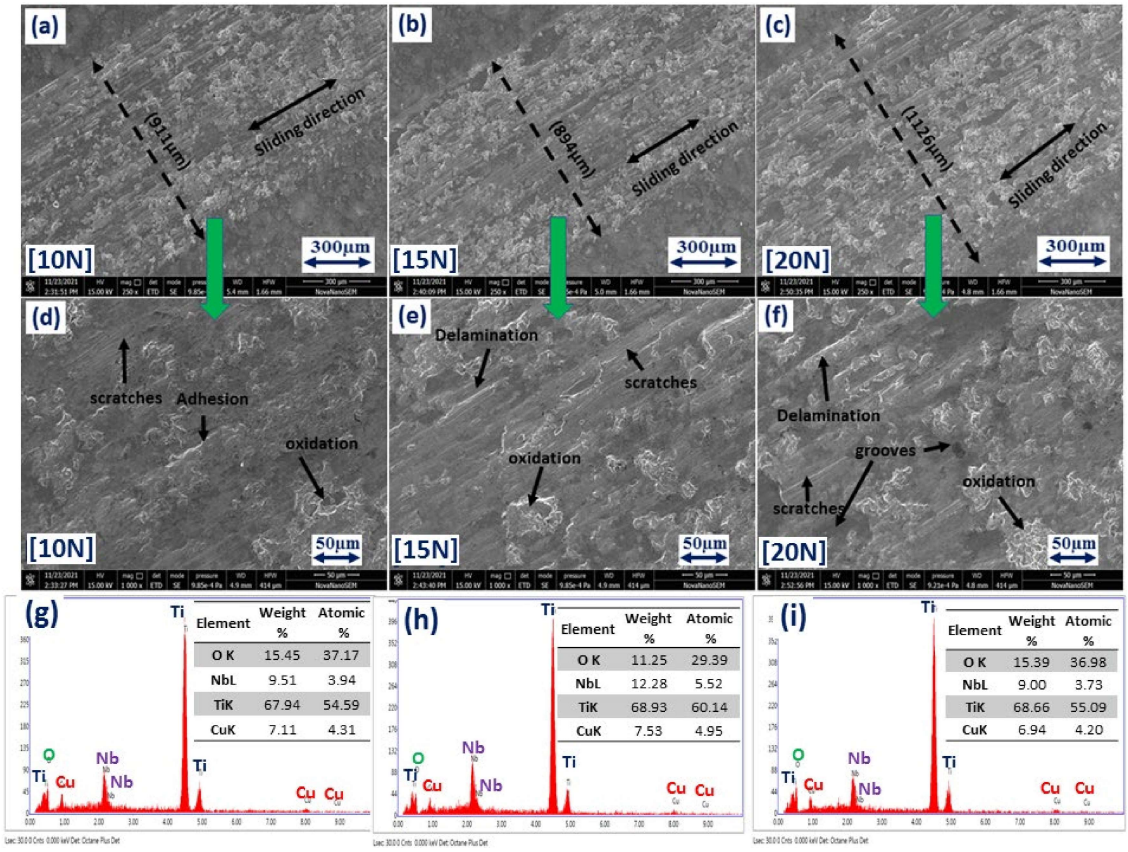

Fig. 5.18- The SEM micrograph and EDS analysis of the worn surface of Ti-5Cu-15Nb at 10 N (a,d,g), 15 N (b,e,h), and 20 N (c,f, i) load after 3600 cycles.

The lowest cof value was recorded for Ti-5Cu-5Nb at 20 N load, while the highest was for Ti-5Cu-10Nb at 15 N load against zirconia ball in SBF. Furthermore, the EDS analysis at the selected point on the worn area was conducted to investigate the reason for the differences in cof value. Figures 5.19 and 5.20 show the EDS analysis at the selected point on worn surface SEM images of Ti-5Cu-5Nb, and Ti-5Cu-10Nb, respectively, at that particular loading conditions. Figure 5.19 (a) shows the SEM image of the worn surface under 20 N load and four different EDS points with varying appearances. The dark grey phase at spot 1 shows the presence of bare titanium. At the same time, wt.% of other elements like O, Nb, and Cu is lower than 10%, indicating the dominant adhesion wear mechanism and corresponding to Ti, Nb, and Cu oxide (Ureña et al., 2018). The EDS analysis of Spot 2 shows the copper-rich phase,

whereas spot 3 shows the oxide of copper and niobium, as the oxygen percentage is higher than spot 2. According to the EDS result, spot 4 is light grey and contains titanium oxide.

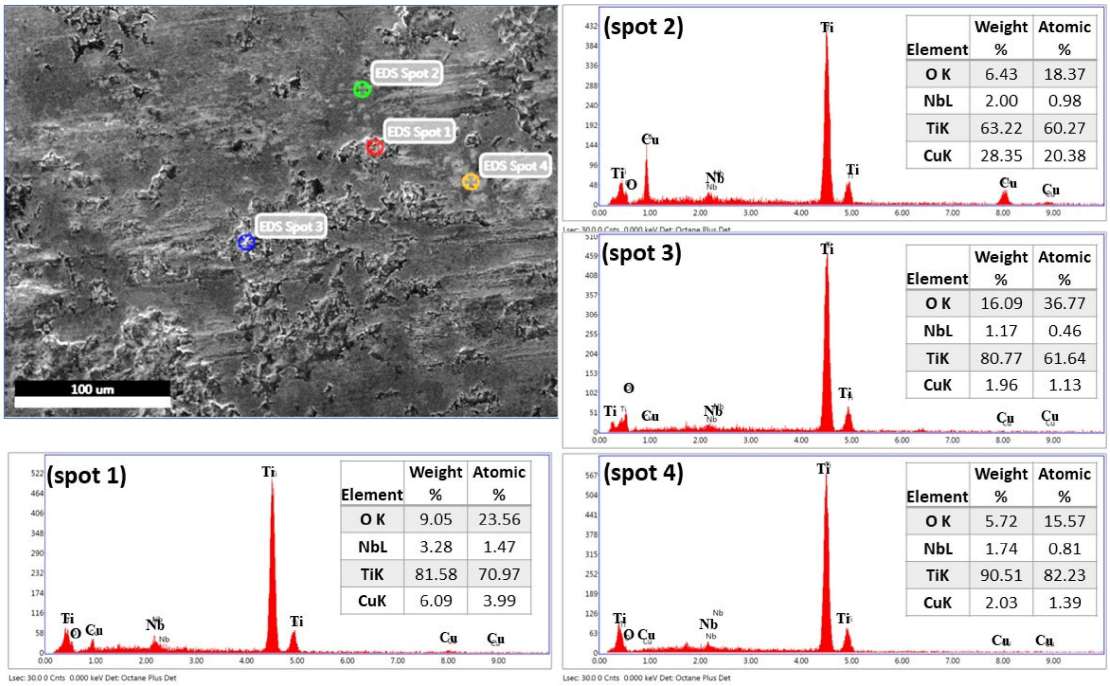

Fig. 5.19- EDS point spectrum analysis of the worn surface of Ti-5Cu-5Nb at 20 N load.

In Fig. 5.20, spot 2 (black phase) shows a less percentage of niobium and copper which further depicts the presence of oxide of both Nb and Cu, while the plane surface at spot 1 represents the copper-rich phase, same as spot 2 of Fig. 5.19. Furthermore, spots 3 and 4 (white color) have a higher percentage of oxygen, indicating the production of oxide due to oxidation, adhesion, and abrasion between the counterpart and sample. The worn surface shows that the grooves and scratches mark parallel to the wear track, a typical example of an abrasive mark cutting mechanism. The abrasion between asperities of sample Ti-5Cu-10Nb and zirconia ball greatly enhances the cof value (Akbarpour & Moniri Javadhesari, 2017).

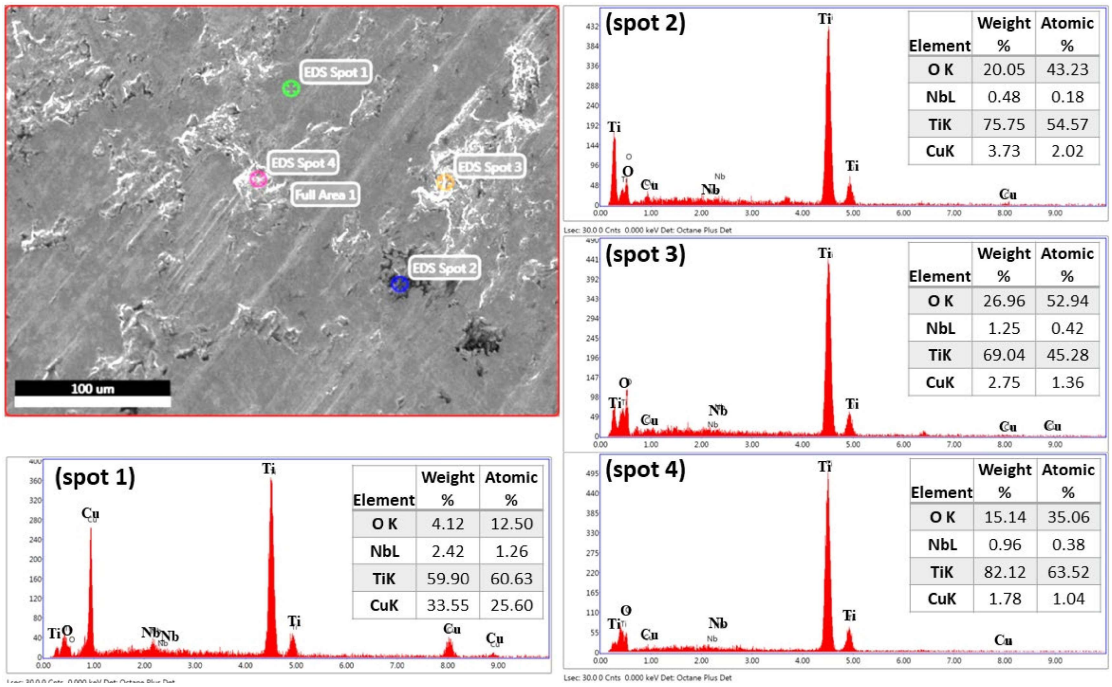

Fig. 5.20- EDS point spectrum analysis of the worn surface of Ti-5Cu-10Nb at 15 N load.

5.3.5 Scanning probe microscope analysis

The maximum and minimum losses in wear volume were observed in Ti-5Cu, and Ti-5Cu-15Nb, respectively, after the wear test. The SPM analysis was used to investigate the effect of surface roughness on volume loss. The linear roughness and surface roughness parameter of the worn surface obtained after SPM analysis by Gwyddion software is shown in Table 5.4. The surface topography of the worn surfaces at different loads of Ti-5Cu and Ti-5Cu-15Nb is shown in Fig. 5.21 and 5.22, respectively. On the worn surface, a 60*60 μm^2 area was taken for study. For Ti-5Cu, the maximum friction coefficient was observed at 10 N load, and the presence of numerous peaks and valleys, as shown in Fig. 5.21 (d) compared to Fig. 5.21 (e and f), proved the same. However, the maximum height of peaks on the worn surface of Fig. 5.21 (d) is the lowest (0.63 µm) compared to the maximum height of the worn surface of Ti-5Cu at 15 N (1.15 µm) and 20 N (1.2 µm) load. The surface topography of the worn surface of sample Ti-5Cu, at 15N load shows the smooth plane in some regions, as shown in Fig. 5.21

(e). The wear volume and wear rate increase with increasing load; also, at 20 N load, the surface topography of the worn surface shows the maximum volume loss. The wear mechanism in the 20 N load shows adhesion, abrasion, and oxidation.

The surface topography of the worn surface of Ti-5Cu-15Nb is shown in Fig. 5.22. The surface roughness of the sample at all three loading conditions is solely different according to the result of wear loss volume. At the 10 N loading condition, the maximum height of the peaks from the valley is lowest compared to 15 N and 20 N loading conditions, as shown in Fig. 5.22 (a). The wear profile of the substrate at 10 N load is parallel to the sliding direction, while the 20 N load is slightly different. This results in a higher friction coefficient at 10 N load than in 15 N loading conditions. However, the wear profile of the substrate at 20 N load is different, and maximum roughness caused the higher cof value. The maximum loss in wear volume was obtained at 20 N loading condition; the peak to valley height for this is maximum compared to others. It can be seen from Fig. 5.22 (f) that the wear profiles of the substrate have deep grooves, sharp edges, delamination, and accumulation of particles; this confirms the material lost by abrasion, adhesion, and oxidation (Lu et al., 2020).

Table 5.4 - The summary of surface roughness of worn surface for different loading.

samples		Line roughness		Surface roughness	
		R_a, nm	R_q, nm	S_a, nm	S_q, nm
Ti-5Cu	10N	19.68	27.18	37.93	56.13
	15N	27.34	48.17	46.40	70.97
	20N	24.07	39.12	28.86	48.89
Ti-5Cu-15Nb	10N	166.47	235.35	381.72	493.75
	15N	154.55	210.36	342.8	459.68
	20N	190.35	256.4	376.12	579.25

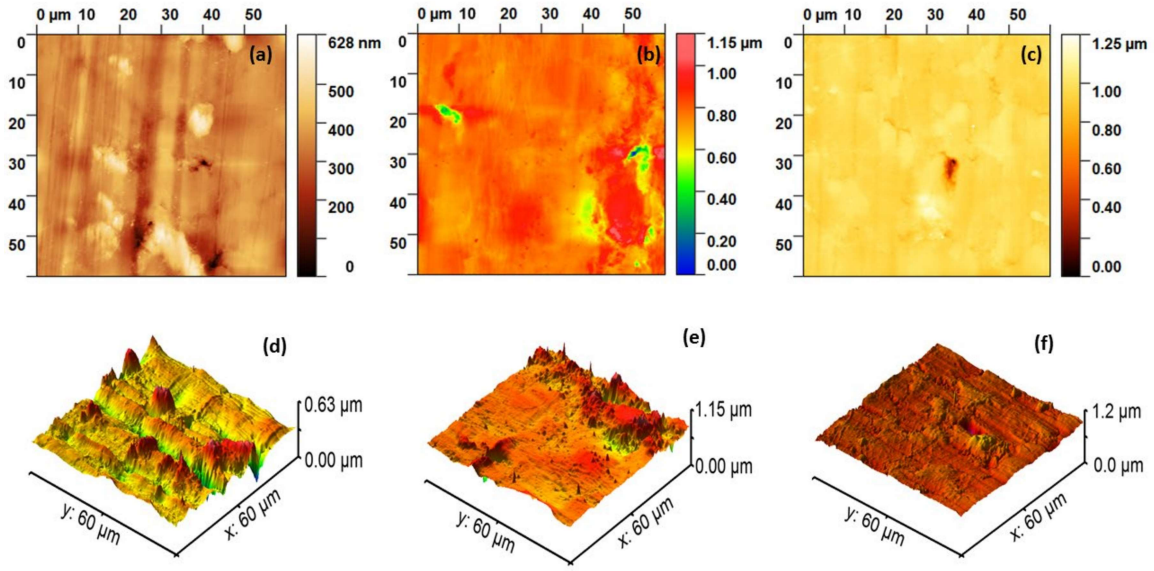

Fig. 5.21- Surface topography of Ti-5Cu alloy at (a) 10 N, (b) 15 N, and (c) 20 N load of worn surface, and images (d), (e), (f) are 3D surface topography, respectively

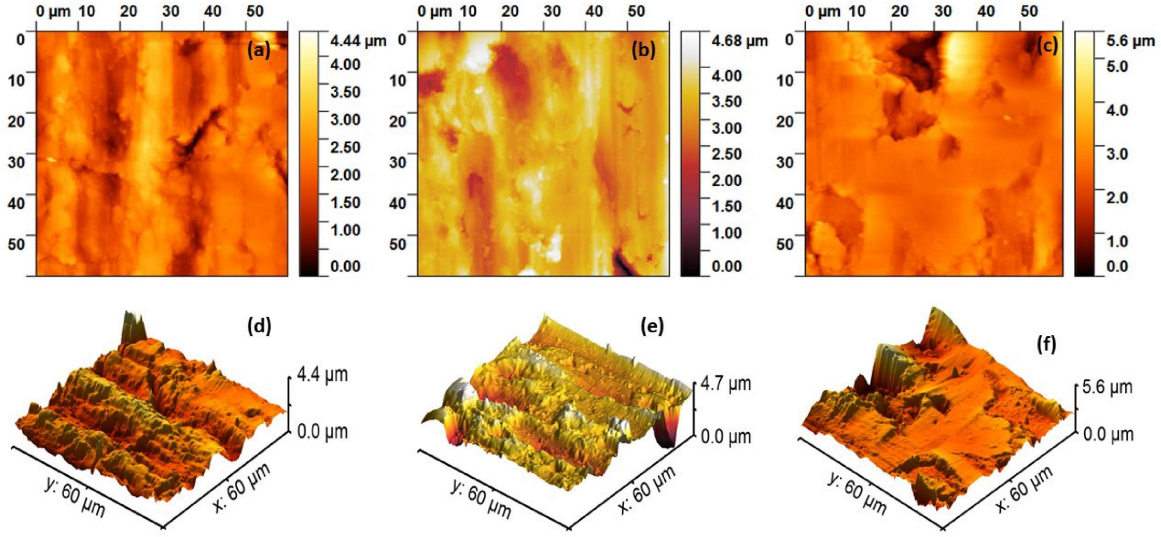

Fig. 5.22- Surface topography of Ti-5Cu-15Nb alloy at (a) 10 N, (b) 15 N, and (c) 20 N load of worn surface, and images (d), (e), (f) are 3D surface topography, respectively.